Microgravity spreading of water spheres on hydrophobic capillary plates

Laura Steub[1], *Jonathan* Kollmer[1], *Derek* Paxson[2], *Achim* Sack[1], *Thorsten* Pöschel[1], *John* Bartlett[2], *Douglas* Berman[2], *Yaateh* Richardson[2], and *Michel Y.* Louge[2,⋆]

[1] *Institute for Multiscale Simulation, Friedrich-Alexander-Universität Erlangen-Nürnberg, Erlangen 91052, Germany*
[2] *Sibley School of Mechanical and Aerospace Engineering, Cornell University, Ithaca, NY 14853, USA*

Abstract. We create nearly perfect centimetric spheres of water by splitting a cavity consisting of two metal hemispheres coated with a hydrophobic paint and under-filled with liquid, while releasing the apparatus in free-fall. A high-speed camera captures how water spread on hydrophobic aluminum and polycarbonate plates perforated with cylindrical capillaries. We compare observations at the ZARM drop tower in Bremen with Lattice-Boltzmann numerical simulations of Frank, Perré and Li for the inertial phase of imbibition.

1 Background

The wetting of porous surfaces is crucial to any application where the three states of matter coexist [1]. When a liquid drop touches a dry porous medium, it spreads as if laid on a composite surface. Specifically, the porous surface first behaves as a hydrophobic material, since the liquid must penetrate pores filled with air. As soon as contact is established, part of the liquid is absorbed by capillary forces that are resisted by viscous losses growing with the length of the imbibed region. This process is complicated by the motion of triple gas-liquid-solid contact lines progressively overcoming each capillary. For simplicity, Cassie and Baxter [2] treated the porous surface as an effective material made up of a solid trapping air cavities. Because this approach did not entirely explain the dynamics of liquid imbibition, later studies also considered the balance of viscous forces and capillarity [3–9].

Imbibition of a liquid sphere of density ρ, viscosity μ, surface tension σ and radius R_i always begins with an inertial regime on a time scale $\tau = (\rho R_i^3/\sigma)^{1/2}$ [10]. The relative importance of bulk liquid inertia and viscous forces on the porous surface is measured by a Reynolds number based on drop size and characteristic capillary invasion speed $u_c \sim \sigma/\mu$, known as the Laplace number $\mathrm{La} \equiv \rho R_i \sigma/\mu^2$. Because $\mathrm{La} \propto 1/\mu^2$, it is large even for tiny water drops, and therefore inertia cannot be ignored.

In that context, Frank, Perré and Li [11, 12] observed the role of inertia in lattice-Boltzmann (LB) numerical simulations without gravity. For simplicity, they neglected contact angle hysteresis [13] and modeled the porous medium as a periodic array of cylindrical capillaries perpendicular to the free surface. By following the evolution of the effective contact angle while resolving flow details in and around capillaries, they found that drop spreading and penetration take place simultaneously. However, to stage a specific viscosity while remaining numerically stable, their LB simulations had to fix the ratio of the temporal increment δ_t and the square of the spatial grid size δ_x [14]. For imbibition, this required $(\delta_t/\tau) \propto (\delta_x/R_i)^2 \mathrm{La}^{1/2}$. Meanwhile, to avoid unphysical compressibility, the LB technique kept the pseudo Mach number $\mathrm{Ma} = u_c \delta_t/\delta_x \propto \mathrm{La}^{3/4}(\delta_t/\tau)^{1/2}$ small by limiting the Laplace number. Despite these challenges, Frank, et al [11, 12] achieved sufficiently high La = 41 or 135 to show that inertia governs imbibition initially by slowing down the rate of decrease in drop height. Once inertia was defeated, they found that drop height decreased at a more rapid rate mitigated by viscous capillary invasion.

Unfortunately, the La values of Frank, et al [11, 12] were smaller than expected. For example, a water drop ($\sigma \simeq 0.072\,\mathrm{J/m^2}$, $\rho = 1000\,\mathrm{kg/m^3}$, $\mu \simeq 8.9.10^{-4}\,\mathrm{kg/m.s}$) of 1 mm diameter has $\mathrm{La} \simeq 4.5.10^4$). Therefore, an objective was to verify that this mismatch was inconsequential. In addition, because pores delay the progression of the air-water interface, we set out to establish whether the contact line pins, as happens at smaller scales [15], particularly with substantial hysteresis between advancing and receding contact angles [16, 17]. To those ends, we designed a microgravity experiment with a drop large enough to resolve details around individual pores. However, we staged solids that turned out to possess hydrophobic advancing angles. Therefore, our results are mainly relevant to the spreading of water on hydrophobic textured surfaces.

We deployed the apparatus at the 4.74 s ZARM microgravity drop tower in Bremen (Germany). After a brief description, we present results and discuss their significance.

2 Experiments

Figure 1 shows components of one of four identical rigs deployed in the payload capsule of the evacuated 120-m

⋆e-mail: Michel.Louge@cornell.edu

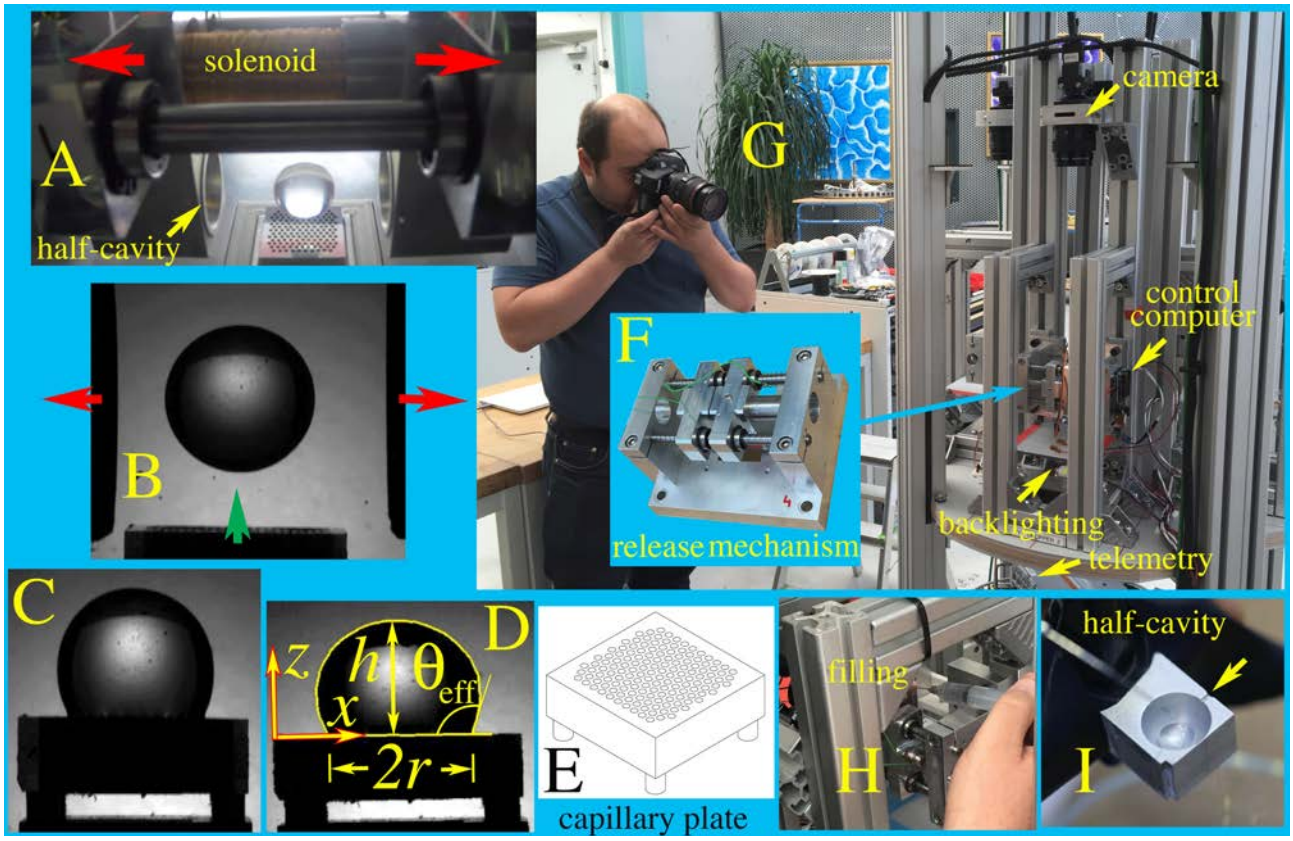

Figure 1. Free-fall apparatus. (A) Viewed by a side camera, the backlit sphere of water just created by the splitting of two hydrophobic hemispherical cavities hovers above the rising capillary plate of aluminum with $\epsilon = 44\%$, while the solenoid coil is extended. (B – D) Typical high-speed frames. Red and green arrows represent direction of motion of cavities and plate, respectively. (C) The drop spreads on the capillary plate. (D) Superimposed computer-generated outlines and notation. (E) Perspective drawing of a $20 \times 20\,\mathrm{mm}^2$ aluminum or polycarbonate plate with 146 cylindrical open capillaries of 1 mm on a triangular lattice at $\epsilon = 44\%$ to 6.4 mm depth. (A plate of similar geometry with $\epsilon = 11\%$ had 46 holes). (F) Close-up of one of the release mechanisms. (G) Overview of the microgravity payload before insertion into ZARM's hermetic capsule, consisting of four identical apparatuses, each with a different capillary plate (Table 1). (H) Filling the cavity of 19 mm diameter with demineralized water using a curved syringe needle on the closed cavity. (I) Prior test of cavity hydrophobicity with a similar water volume in one of the hemispheres; the arrow points to the filling channel.

free-fall tower. Before sealing the hermetic capsule, demineralized water was introduced to fill roughly 40% of each spherical cavity treated with a hydrophobic coating (e.g. Rust-Oleum® NeverWet®, contact angle $\simeq 154\,^\circ$). Underfilling the cavity was essential to let air insinuate itself under the nascent drop and produce a nearly perfect water sphere (radial distortion $\delta R_i/R_i < 2\%$, see Table 1).

In a sequence optimized by trial and error, an Arduino UNO microcontroller delayed cavity opening by 2 s after onboard telemetry detected free-fall to let water relax before splitting the cavity. It then triggered the video camera (2000 fps, 512×512 pixels), and turned on LED backlighting last to avoid heating. To split the cavity rapidly without vibration, we designed a mechanism consisting of a solenoid tighly-wound around a permanent neodymium bar magnet, linear bearings, springs and shock absorbers. Once a nearly perfect water sphere hovered motionless, an actuator raised a capillary plate to meet it. We tested plates made up of polycarbonate or aluminum, pierced with open-ended cylinders of 1 mm diameter on periodic triangular arrays with opening surface fraction $\epsilon = 44\%$ or 11%. Separate measurements on a Rame-Hart 500 Goniometer established that the aluminum had advancing and receding contact angles $\theta_a = 93.5 \pm 1.6\,^\circ$ and $\theta_r = 82.6 \pm 2.2\,^\circ$, respectively, while the polycarbonate had $\theta_a = 103 \pm 5\,^\circ$ and $\theta_r = 90 \pm 2\,^\circ$.

As Fig. 1D shows, the Image Processing Toolbox of MATLAB recorded left and right drop outlines at distances $x_{\min} \equiv \min(x)$ and $x_{\max} \equiv \max(x)$ parallel to the plate and altitude z above it. We also recorded time-histories of drop height $h \equiv \max(z)$ and contact patch radius $r \equiv (x_{\max} - x_{\min})/2$ at $z = 0$. Because the actuator was operated by the microcomputer in open-loop, the plate reached the water sphere with a finite speed u_0 that produced waves. Unfortunately, the absence of images from different camera orientations prevented us from calculating the water volume V above the plate with precision. Instead, we exploited the instantaneous drop outline to find the estimate

$$V \simeq \int_{z=0}^{h} \frac{\pi}{4} \left(x_{\max} - x_{\min}\right)^2 \mathrm{d}z, \qquad (1)$$

which was subject to artificial oscillations as the drop surface lost instantaneous axisymmetry.

3 Results

In a typical test, nearly perfect water spheres were met by the capillary plate, thus initiating a rapid spread illustrated as time-histories of contact patch radius in Fig. 2. The contact line pinned at times $\sim \tau$, marking the end of the spreading phase. Slowly-decaying oscillations, which remained after plate and water touched, later reflected downward, allowing us to trace the effective advancing and receding contact angles $\theta_{a,\mathrm{eff}}$ and $\theta_{r,\mathrm{eff}}$ on the textured surface.

As Table 1 and Fig. 2 show, hardly any water penetrated capillaries, as expected for the hydrophobic advancing angles that our solids turned out to possess. For a pinned spherical cap with $\theta_{a,\mathrm{eff}}$, a reduction δV in initial volume V_i (Table 1) would imply a mean imbibition depth

$$\bar{d} = \frac{3R_i}{8 \times 2^{1/3}\epsilon}\left(\frac{\delta V}{V_i}\right)\frac{(2 - 3\cos\theta_{a,\mathrm{eff}} + \cos^3\theta_{a,\mathrm{eff}})^{2/3}}{\sin^2\theta_{a,\mathrm{eff}}}, \quad (2)$$

or $\bar{d} \simeq 0.5$ mm for Al at $\epsilon = 44\%$, 1.7 mm for Al at $\epsilon = 11\%$, and 0.3 mm for PC at $\epsilon = 44\%$. Therefore, our experiments chiefly tested spreading of water spheres on hydrophobic textured surfaces in the absence of gravity.

Frank, et al [11, 12] fitted such inertial spreading of the contact patch of radius r to the power law

$$\frac{r}{R_i} \simeq C\left(\frac{t}{\tau}\right)^{\alpha}. \quad (3)$$

Figure 2 illustrates similar fits of our data, with constants summarized in Table 1. Figures 3 and 4 compare these results to simulations that Frank, et al [12] conducted without capillaries ($\epsilon = 0$) at different values of $\theta_a = \theta_r$. The agreement implies that the effective advancing contact angle conformed to the model that they recommended,

$$\cos\theta^{\mathrm{mod}}_{\mathrm{a,eff}} = (1 - \epsilon)\cos\theta_a - \epsilon, \quad (4)$$

so long as capillaries were hardly invaded. As Table 1 shows, measurements of $\theta_{a,\mathrm{eff}}$ also support this Cassie-Baxter expression. The data suggest a similar relation for

$$\cos\theta^{\mathrm{mod}}_{\mathrm{r,eff}} = (1 - \epsilon)\cos\theta_r - \epsilon. \quad (5)$$

In short, this behavior of textured surfaces on hydrophobic solids is consistent with the Cassie-Baxter description [2], which Louge [18] identified as the last of six equilibrium regimes of the hysteretic contact line. In regime VI, the internal surface of a cavity on a hydrophobic solid is large compared with its opening, while adjacent cavities remain unconnected [18]. Further microgravity experiments with hydrophilic solids should be conducted to explore adjacent regimes and test whether drop spreading would behave differently.

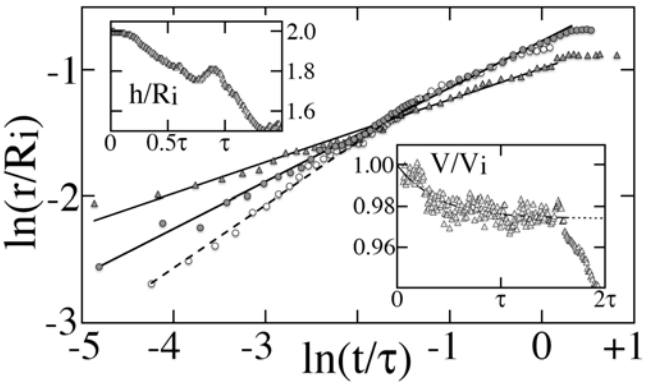

Figure 2. Time histories of $\ln r/R_i$ vs $\ln t/\tau$. Symbols and conditions, see Table 1. Right and left insets show, vs increments in τ, relative volume V/V_i inferred from Eq. (1) and, for the polycarbonate marked by an asterisk in Table 1, relative height h/R_i, before oscillations engulf the entire drop.

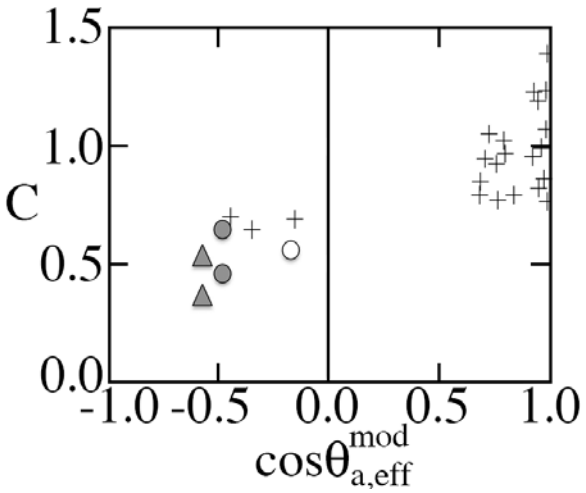

Figure 3. Coefficient C in the power law fit of Eq. (3) vs cosine of the effective advancing contact angle calculated from Eq. (4) and independent measurements of θ_a on the goniometer. Plus signs are from the numerical simulations of Frank, et al. [12] with $\epsilon = 0$ (flat plate). Symbols and conditions, see Table 1.

Acknowledgements

DP and MYL were supported by NPRP grant 6-059-2-023 of the Qatar National Research Fund; LS, JK and TP by the German Science Foundation via the Cluster of Excellence Engineering of Advanced Materials; and LS through the ESA Education 'Drop Your Thesis!' program. The authors are grateful to the ZARM staff, to Nigel Savage, Lily Ha and Lucas Pfeiffer of ESA Education, and to Florian Fuchs for help with experiments, to Patrick Perré, Xavier Frank, Hervé Duval and Floran Pierre for illuminating discussions, to Jin Xu, Carlos Mejia, Nicole Panega, Gilbert Hegermiller, Rukang Huang, Seetha Kolli and Richard Goodwyn for help designing the microgravity payload, and to Anshuman Das and Keya Gangadharan for measuring contact angles with NSF CBET 1637531 support.

References

[1] J. H. Snoeijer, and B. Andreotti, Annu. Rev. Fluid Mech. **45**, 269–292 (2013)

[2] A. B. D. Cassie, and S. Baxter, Trans. Faraday Soc. **40**, 546–551 (1944)

Table 1. Experimental conditions and results for plates made up of solids shown (Al = aluminum, PC = polycarbonate) with capillary surface fraction ϵ (%) at the surface $z = 0$. V_i (ml) and $\delta R_i/R_i$ are, respectively, initial volume of the suspended water sphere and fractional discrepancy in its radii along x and z. u_0 (cm/s) is relative velocity of sphere and plate at impact, persisting until the plate stops at time t_s relative to the inertial time τ. $\delta V/V_i$ is the ultimate visible fraction of water imbibed into capillaries, inferred through Eq. (1), and fitted using a decaying exponential as shown in the right inset of Fig. 2. The constants C and α are fitted to Eq. (3), as shown in Fig. 2. $\theta_{\rm a,eff}$ and $\theta^{\rm mod}_{\rm a,eff}$ are, respectively, the effective advancing contact angle measured once the drop is pinned, and its prediction of Eq. (4) with θ_a independently measured on the goniometer. $\theta_{\rm r,eff}$ and $\theta^{\rm mod}_{\rm r,eff}$ are their receding counterparts, see Eq. (5).

solid		ϵ	V_i	$\delta R_i/R_i$	u_0	t_s/τ	$\delta V/V_i$	C	α	$\theta_{\rm a,eff}$	$\theta^{\rm mod}_{\rm a,eff}$	$\theta_{\rm r,eff}$	$\theta^{\rm mod}_{\rm r,eff}$
Al	●	44	1.26	2.0%	3.1	1.2	3.6 ± 2%	0.65	0.52	118°	118 ± 1°	110°	112 ± 1°
Al	●	44	1.13	0.2%	3.2	1.7		0.46	0.37	116°	118 ± 1°	100°	112 ± 1°
Al	○	11	1.45	0.2%	2.7	0.74	4.7 ± 3%	0.56	0.50	93°	99 ± 2°	93°	90 ± 2°
PC*	▲	44	1.25	1.4%	3.0	1.4	2.6 ± 2%	0.37	0.25	124 ± 1°	125 ± 3°	109 ± 3°	116 ± 2°
PC	▲	44	1.28	0.2%	4.5	0.99		0.54	0.34	110 ± 2°	125 ± 3°	91 ± 1°	116 ± 2°

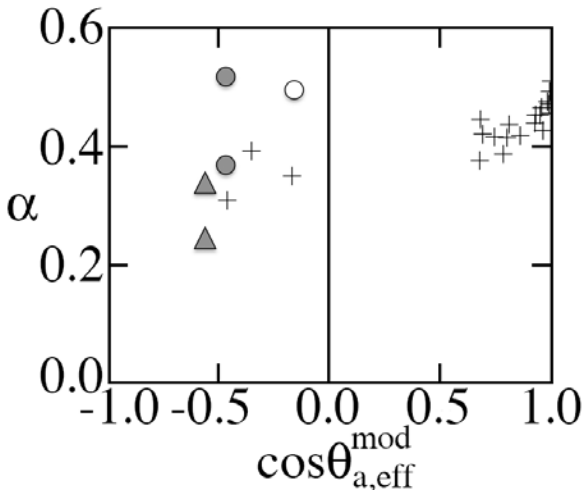

Figure 4. Exponent α in Eq. (3) vs $\cos\theta_{\rm a,eff}$ in Eq. (4). Symbols and conditions, see Fig. 3.

[3] M. Denesuk, G.L. Smith, B.J.J. Zelinski, N.J. Kreidl, and D.R. Uhlmann, Coll. Interface Sci. **158**, 114–120 (1993)

[4] M. Denesuk, B.J.J. Zelinski, N.J. Kreidl, and D.R. Uhlmann, Coll. Interface Sci. **168**, 142–151 (1994)

[5] V. M. Starov, S.A. Zhdanov, and M.G. Velarde, Langmuir **158**, 9744–9750 (2002)

[6] V. M. Starov, S.A. Zhdanov, S.R. Kosvintsev, V.D. Sobolev, and M.G. Velarde, Adv. Colloid Interface Sci. **104**, 123–158 (2003)

[7] S. H. Davis, and L.M. Hocking, Phys. Fluids **11**, 48–57 (1999)

[8] S. H. Davis, and L.M. Hocking, Phys. Fluids **12**, 1646–1655 (2000)

[9] A. Clarke, T.D. Blake, K. Carruthers, and A. Woodward, Langmuir **18**, 2980–2984 (2002)

[10] J. C. Bird, S. Mandre, and H. A. Stone, Phys. Rev. Lett. **100**, 234501 (2008)

[11] X. Frank, and P. Perré, Phys. Fluids **24**, 042101 (2012)

[12] X. Frank, P. Perré, and H.-Z. Li, Phys Rev. E **91**, 052405 (2015)

[13] D. Quéré, Annu. Rev. Mater. Res., **38**, 71–99 (2008)

[14] R. R. Nourgaliev, T. N. Dinh, T. G. Theofanous, and D. Joseph, Int. J. of Multiphase Flow, **29**, 117–169 (2003)

[15] C. Priest, T.W.J. Albrecht, R. Sedev, and J. Ralston, Langmuir **25**, 5655–5660 (2009)

[16] R. E. Johnson, and R. H. Dettre, J. Phys. Chem. **68**, 1744–1750 (1964)

[17] E. Schäffer, and P.-Z. Wong, Phys Rev. E **61**, 5257–5277 (2000)

[18] M. Y. Louge, Phys Rev. E **95**, 032804 (2017)